Optics and Lasers in Engineering 173 (2024) 107900

Contents lists available at ScienceDirect

Optics and Lasers in Engineering

journal homepage: www.elsevier.com/locate/optlaseng

Polarization-sensitive optical coherence tomography for renal tumor detection in *ex vivo* human kidneys

Feng Yan [a], Chen Wang [a], Yuyang Yan [a], Qinghao Zhang [a], Zhongxin Yu [b], Sanjay G. Patel [c], Kar-Ming Fung [b,d], Qinggong Tang [a,e,*]

[a] Stephenson School of Biomedical Engineering, University of Oklahoma, Norman, OK 73019, United States
[b] Department of Pathology, University of Oklahoma Health Sciences Center, Oklahoma City, OK 73104, United States
[c] Department of Urology, University of Oklahoma Health Sciences Center, Oklahoma City, OK, United States
[d] Stephenson Cancer Center, University of Oklahoma Health Sciences Center, Oklahoma City, OK 73104, United States
[e] Institute for Biomedical Engineering, Science, and Technology (IBEST), University of Oklahoma, Norman, OK 73019, United States

ARTICLE INFO

Keywords:
Polarization-sensitive optical coherence tomography
Kidney cancer
Renal tumor
Tumor border
Surgical guidance

ABSTRACT

Kidney cancer is a kind of high mortality cancer because of the difficulty in early diagnosis and the high metastatic dissemination in treatments. The surgical resection of tumors is the most effective treatment for renal cancer patients. However, precise assessment of tumor margins is a challenge during surgical resection. The objective of this study is to demonstrate an optical imaging tool in precisely distinguishing kidney tumor borders and identifying tumor zones from normal tissues to assist surgeons in accurately resecting tumors from kidneys during the surgery. 30 samples from six human kidneys were imaged using polarization-sensitive optical coherence tomography (PS-OCT). Cross-sectional, *enface*, and spatial information of kidney samples were obtained for microenvironment reconstruction. Polarization parameters (phase retardation, optic axis direction, and degree of polarization uniformity (DOPU) and Stokes parameters (Q, U, and V) were utilized for multi-parameter analysis. To verify the detection accuracy of PS-OCT, H&E histology staining and dice-coefficient were utilized to quantify the performance of PS-OCT in identifying tumor borders and regions. In this study, tumor borders were clearly identified by PS-OCT imaging, which outperformed the conventional intensity-based OCT. With H&E histological staining as golden standard, PS-OCT precisely identified the tumor regions and tissue distributions at different locations and different depths based on polarization and Stokes parameters. Compared to the traditional attenuation coefficient quantification method, PS-OCT demonstrated enhanced contrast of tissue characteristics between normal and cancerous tissues due to the birefringence effects. Our results demonstrated that PS-OCT was promising to provide imaging guidance for the surgical resection of kidney tumors and had the potential to be used for other human kidney surgeries in clinics such as renal biopsy.

1. Introduction

The kidney cancer that arises in the renal parenchyma is mainly adenocarcinoma, also known as renal cell carcinomas (RCCs) [1]. RCCs comprise a heterogeneous group of cancers with different genetic and molecular alterations [2]. Almost a third of all patients with kidney tumors have metastatic dissemination at clinical diagnosis and nearly half of all patients die from the tumor [3]. There are about 79,000 cases of kidney cancer will be diagnosed and 13,920 cases will die in 2022 according to the most recent estimation from the American Cancer Society. Only 10 % of kidney cancer patients present with the classic triad of symptoms: hematuria, flank pain, and palpable masses. Most cancer cases can be diagnosed or incidentally found on magnetic resonance imaging (MRI), computed tomography (CT) scan, or ultrasound [4,5]. The systemic therapy plan for the kidney tumor such as surgically resection and ablation, percutaneously biopsied and immunohistochemically (IHC), depends on patient characteristics and extent of the cancer [4].

Surgical resection is a main treatment that is currently used for small renal masses with benign or malignant tumors in most patients [6,7]. With the early detection and pathologic histology of the kidney tumor, the resection of localized tumorous masses is the most effective

* Corresponding author.
E-mail address: qtang@ou.edu (Q. Tang).

https://doi.org/10.1016/j.optlaseng.2023.107900
Received 27 December 2022; Received in revised form 12 September 2023; Accepted 15 October 2023

treatment for patients. To accurately resect the localized kidney tumor at an early stage and maximally decline the risk of distant metastases, the precise detection of tumorous regions and margins plays an important role in the surgery. Standard imaging tests including MRI, CT, and ultrasound are main screening modalities currently utilized for characterizing the mass size, possible abdominal metastases, tumor extension, and venous involvement for staging [2]. Although macroscopic imaging methods such as MRI and CT allow for the evaluation of kidney tumor extension at advanced stage, localizing small kidney tumors at early stage is still difficult because of relatively lower spatial resolutions [8–11]. MRI and CT have no advantage for precise surgical guidance to resect small kidney tumors under retaining patient's normal kidney tissues. Although ultrasonography was able to provide real-time observation of ablated tissues [12], the main aim of ultrasound imaging was to focus on the diagnosis and treatment monitoring of big kidney tumors at advanced stage [13,14]. The accurate differentiation and localization of small kidney tumors by ultrasonography were limited due to the low resolution (150 μm in high-resolution ultrasound imaging system) [15]. In summary, the primary challenges that surgeons are facing in renal tumor resection surgeries are: 1) finding an imaging tool for real-time guiding the resection of tumor tissues during the surgery; and 2) obtaining high-resolution images from the real-time imaging to segment tumor margins and profiles. Therefore, there is a critical need to develop a high-resolution imaging modality to provide real-time tumor region and margin distinguishments for renal tumor resection surgery.

Optical coherence tomography (OCT) uses a low-coherence interferometer to produce noninvasive two-dimensional and three-dimensional images with high resolution (~10 μm) for tissue microstructures in vivo and *ex vivo* [16]. Current OCT techniques have been widely reported in cancer/tumor diagnoses and anti-cancer drug screenings [17–21]. However, one of the limitations of conventional intensity-based OCT system is the lack of the tissue-specific contrast thus it is still often difficult to directly differentiate different tissues [22]. Boer and Nelson et al. utilized a polarizer between the low-coherence laser and beam splitter in spectral domain OCT system to build a polarization sensitive OCT system (PS-OCT) that can achieve the differentiation of different internal tissue microstructures based on the optical phase delay and polarization state [23]. Compared to traditional intensity-based OCT modes for structural imaging, PS-OCT provides additional tissue specific contrasts to avoid the ambiguity with image interpretation within internal structures and achieves the quantitative information of different tissues [22]. The biologic tissues with different birefringence property cause unequal propagation speed of differently polarized light. Therefore, PS-OCT is applied to characterize samples by analyzing those changing light polarizations. Because traditional imaging guidance techniques cannot distinguish regions of tumor from admixed contaminant fibrotic stroma, PS-OCT is used to measure the correlation of collagen content in matched histological staining for lung cancer [24]. The study demonstrated that PS-OCT enabled accurate fibrosis detection and distinguished tumor regions with low fibrosis in human lung carcinoma *ex vivo*. Moreover, Strasswimmer and Duan et al. indicated that PS-OCT was a potentially useful tool to examine human and mice skin cancer (basal cell carcinoma) based on the dermal birefringence between normal skin structure and cancerous tissues [25–27]. To improve the accuracy of brain tumor resection, PS-OCT has been demonstrated to precisely delineate the boundary between brain tumor and normal brain tissues due to the capability of PS-OCT for differentiating glioma from white matter [28]. Furthermore, South et al. reported that PS-OCT was able to provide enhanced contrast between healthy and cancerous breast tissues indicating PS-OCT as a potential tool for intraoperative tumor margin evaluation [29]. These studies demonstrate that PS-OCT has significant potential for clinical impact in tumor recognition. Because of the ability to distinguish tumors by detecting the birefringence from fibrosis or collagen, PS-OCT can be applied to guide intraprocedural tissue sampling in vivo or achieve rapid biopsy adequacy assessment. Therefore, PS-OCT can serve as a potentially effective imaging tool to differentiate tumor margins and profile tumor regions via fibrosis detection to provide clinical surgical guidance for renal cancer resection.

The purpose of this study was to use PS-OCT to accurately differentiate the margin of kidney tumors and position multi-dimensional tumorous profiles and regions in renal surgical resection. Herein, we applied a label-free PS-OCT system to qualitatively and quantitatively distinguish and position tumor margins and profiles using several polarization parameters including polarization retardation, optic axis direction, and degree of uniformity to guide surgical resection of tumorous tissues in fresh *ex-vivo* human kidneys. In particular, we characterized tumor margins of cross-sectional and *enface* directions by utilizing 2D XZ (front to back vision)/YZ (left to right vision) and XY (top to bottom vision) structural parameter images. We showed that PS-OCT provided accurate and robust differentiation between normal and cancerous kidney tissues. Moreover, we demonstrated the ability of 3D PS-OCT to provide the spatial information of tumor structure within human kidneys based on multi-parameter structural images in different depths and surfaces, offering the availability to position and track the spatial structure of tumor during the kidney resection surgery. Our results demonstrated that PS-OCT is a promising tool to accurately detect and differentiate tumorous tissues from normal tissues within human kidneys. Overall, PS-OCT possesses wide prospects for clinical applications in kidney cancer resection surgeries.

2. Methods and materials

2.1. Sample preparation and ethics committee approval

This study was approved by the University of Oklahoma and the University of Oklahoma Health Sciences Center Institutional Review Board (IRB) (Study number: IRB #12462 and IRB #14794). All the experiment-used human kidney samples were preserved by hypothermic machine perfusion (HMP) for keeping the kidney sample's physiological status and imaged within 2 days after removing from the donors and patients. Six human kidneys with renal tumors and without other kidney diseases were used in the study. Five locations in each kidney subject were selected for PS-OCT imaging .

2.2. Histology staining

To verify the accessibility and accuracy of PS-OCT imaging for kidney tumor, the regions of human kidney tissues were excised and processed for histological staining after PS-OCT imaging to compare with corresponding PS-OCT results. The resected kidney tissues were fixed with 10 % formalin, embedded in paraffin, then sectioned (4μm thick) and stained with hematoxylin and eosin (H&E) for histological analysis. Sectioning and H&E staining was manipulated and finished by the Tissue Pathology Shared Resource, Stephenson Cancer Center (SCC), University of Oklahoma Health Sciences Center. Histological images were taken by Keyence Microscope BZ-X800 (*BZ-X series, Itasca, IL, USA*). The H&E staining dye (*Hematoxylin cat#3801571 and Eosin cat# 3,801,616*) was purchased from Leica biosystems (*Deer Park, IL, USA*) and the histology staining was performed using Leica ST5020 Automated Multistainer (*Deer Park, IL, USA*) following the H&E staining protocol at the SCC Tissue Pathology core.

2.3. PS-OCT schematic

Fig. 1 shows a schematic of the integrated PS-OCT system used in imaging the *ex vivo* human kidneys. The broadband light with a center wavelength of 1300 nm and a spectral bandwidth of 100 nm generates a vertical linearly polarized light. The linearly polarized light is then coupled into the polarization maintaining fibers and is further split into reference and sample arms by a beam splitter (BMS). The linearly polarized light in the reference arm passes through a zero-order quarter-

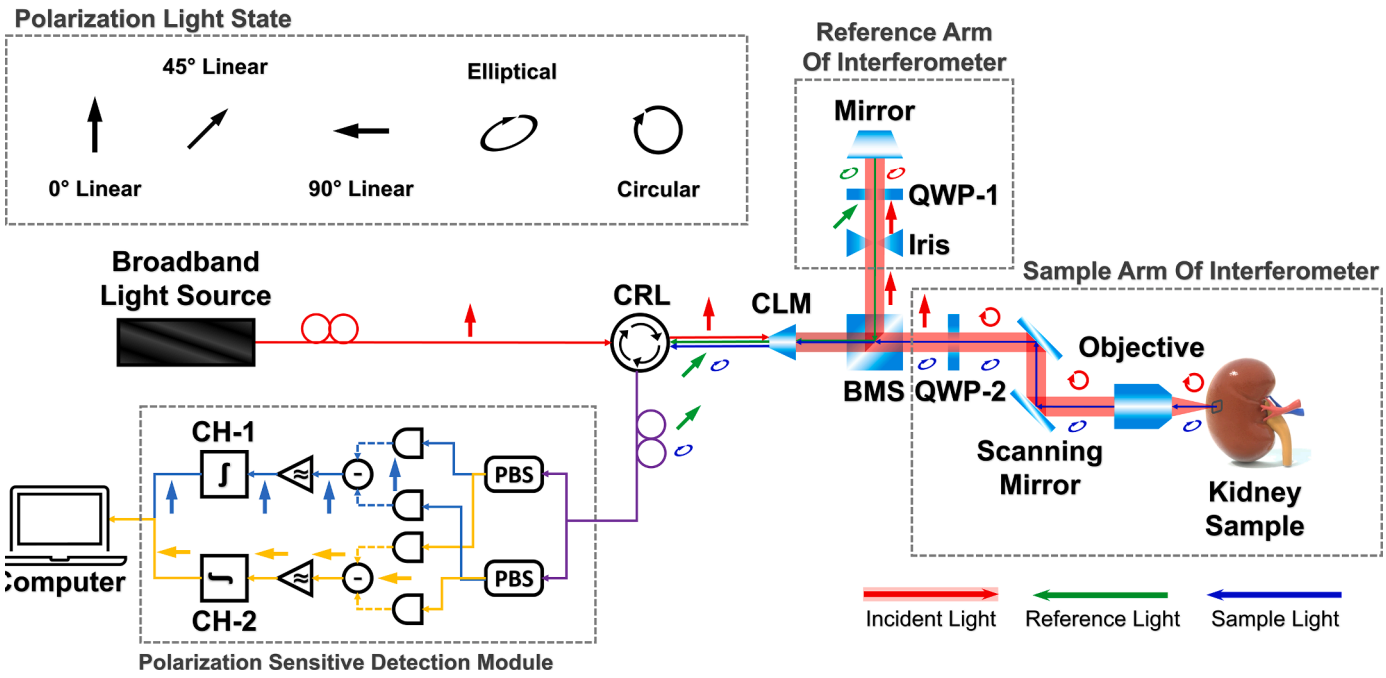

Fig. 1. System schematic of polarization-sensitive optical coherence tomography (PS-OCT) for kidney tumor imaging. Broadband Light Source, 1300 nm center wavelength linear-polarized light. CRL, circulator. CLM, fiber-to-free-space collimator. BMS, beam splitter. Iris, adjustable iris. QWP-1, quarter-wave plate (22.5° orientation). QWP-2, quarter-wave plate (45° orientation). PBS, polarization-sensitive beam splitter. CH-1, channel-1 sensor. CH-2, channel-2 sensor. Sample Arm of Interferometer, incident circular light – equal light amplitude in both orthogonal polarizations, backscattered and reflected elliptical light – encoded polarization and intensity information.

wave plate (QWB-1) with 22.5° orientation and exits with a 45° linear polarization after passing through QWB-1 twice. In the sample arm, the polarized light passes through the zero-order quarter-wave plate (QWB-2) oriented at 45° and is converted into circularly polarized light. The polarized light reflected and scattered by the sample in the sample arm becomes an elliptical polarization state after passing through QWB-2. The recombination of the polarized light in both arms of the system is split into the vertical linearly polarized signal and horizontal linearly polarized signal by two polarization-sensitive beam splitters (PBS), which are detected and processed by two polarization-sensitive channel sensors (CH-1, CH-2) [23,30,31]. The sensitivity of the system at 48 kHz A-scan rate was 105 dB, and the axial and lateral resolutions were 5.5 μm

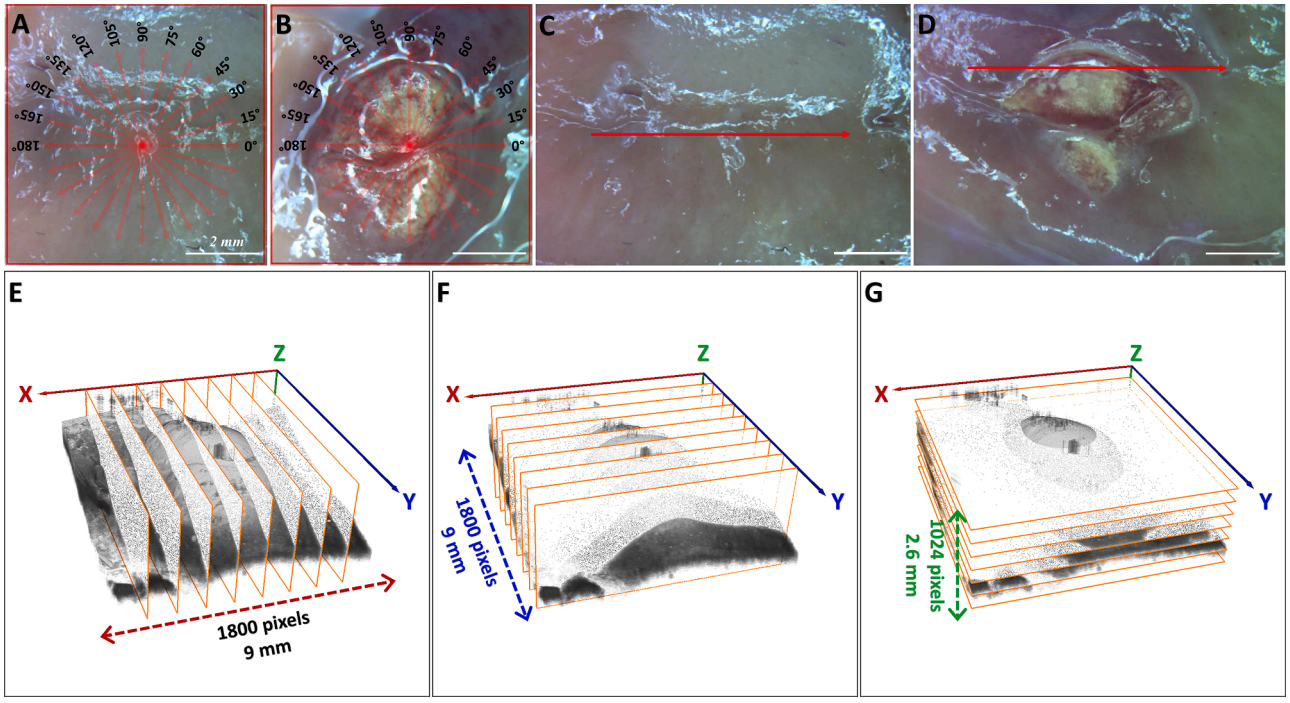

Fig. 2. Scanning and measurement strategy of PS-OCT in 2D and 3D modes. A and C, normal kidney tissue. B and D, cancerous renal tissue. E, 2D YZ cross-sectional slice mode in 3D PS-OCT imaging. F, 2D XZ cross-sectional slice mode in 3D PS-OCT imaging. G, XY *enface* slice mode in 3D PS-OCT imaging.

and 13 μm in air, respectively.

2.4. Measurement

Tumorous tissue and normal tissue from the kidneys were sectioned to be exposed for PS-OCT imaging. The sectioned tissues (cancerous and normal) were kept in the perfusate for keeping tissue physiological functions during the imaging. 2D PS-OCT scanning with a length of 9 mm was used to obtain cross-sectional structure images at 12 different angles (red line arrows in normal tissue (Fig. 2A and 2C) and cancerous tissue (Fig. 2B and 2D), 0 – 180° with a 15-degree step of clockwise) for labeling tumor margin. 3D scanning with a field of view (FOV) of 9 × 9 mm^2 (red frames in Fig. 2A and 2B) was utilized to obtain the volumetric structure and *enface* profile of the samples. 1800 × 1800 × 1024 pixels were set on the length, width, and depth of the 3D PS-OCT imaging, as shown in Fig. 2E-G. The sampling resolutions were 5 × 5 × 2.5 μm^3 in XZ (cross-sectional), YZ (cross-sectional), and XY (*enface*) directions of a 9 × 9 × 2.6 mm^3 volumetric rendering data.

2.5. Data and image processing

In this study, the multi-dimensional structural reconstruction of OCT intensity and PS-OCT information were completed by ImageJ Fiji (*ImageJ 1.53q, Bethesda, MD, USA*) and Amira (*Amira 2021.1, Thermo Fisher Scientific, Agawam, MD, USA*). The data statistics and analyses were performed using GraphPad (*Prism 9.3.1, GraphPad, San Diego, CA, USA*) and Python (*Python 3.10.1, Python Software Foundation, Fredericksburg, VA*) coding. To characterize and quantify the polarization information induced by light-tissue interactions, phase retardation, optic axis orientation, and degree of polarization uniformity (DOPU) based on Stokes vectors and Mueller matrices formalism [32] were used to distinguish tumor regions. Phase retardation and optic axis orientation were determined via the phase difference and the direction of the eigenvalue and eigenvector of the Jones matrix [22], respectively. The phase retardation was aliased into a 0 to π/2 rad range and the optic axis was ranged from -π/2 to π/2 in the angular direction. DOPU was a quantitative measurement of polarization properties of tissues via Stokes vector elements to indirectly quantify the polarization of light. The DOPU value equaled to 1 meaning the single speckle light was fully polarized whereas 0 meaning none polarized. Three Stokes parameters (Q, U, V describing the proportion of polarization state of light corresponding to linear polarization, circularly polarization, and elliptical polarization lights, respectively) were also used to provide the margin detection of tumors. To compare the detection effectiveness between conventional OCT intensity attenuation contrast and PS-OCT, an attenuation coefficient algorithm based on the Beer-Lambert law [33] was applied on OCT intensity images to detect tumor regions. The Dice's coefficient was used to describe the degree of agreement between the histology and PS-OCT data. A score of 1 presented a complete agreement and a score of 0 presented no agreement. The unpaired student *t*-test was performed in the quantitative statistics. A *P*-value of < 0.05 was employed to present the statistical significance between the comparison.

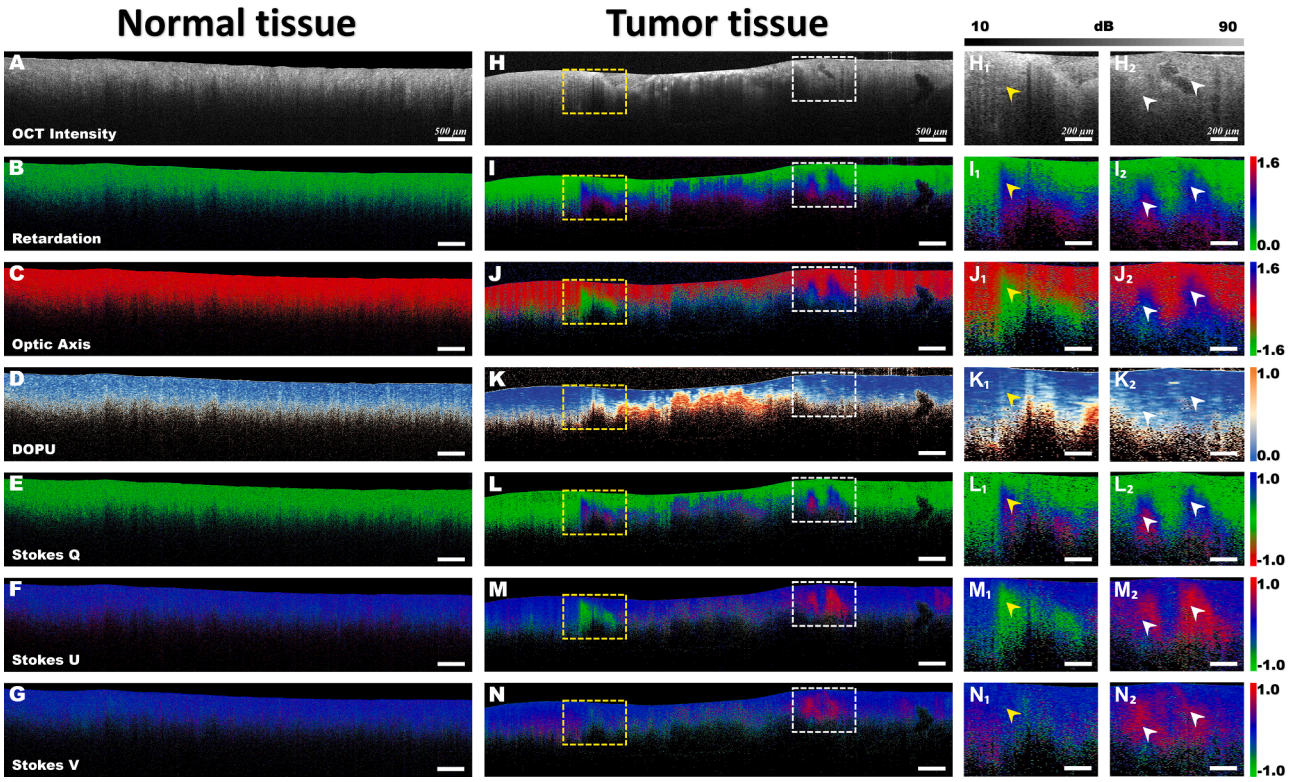

Fig. 3. Representative cross-sectional PS-OCT images of normal and cancerous kidney tissues in intensity and polarization modes. A-G, OCT intensity and polarization images of normal kidney tissues. H—N, OCT intensity and polarization images of cancerous kidney tissues. H_1—N_1, zoomed in sub-images of the left margin of tumor tissues in OCT intensity and polarization modes. H_2—N_2, zoomed in sub-images of the right margin of tumor tissues in OCT intensity and polarization modes. In retardation parameter images, 0.0 represented no phase retardation of light in tissues and 1.6 represented a π/2 phase retardation of light in tissues. Value 1.6 and −1.6 in optic axis images separately represented the optic axis of backward scattered signal from tissues locate on π/2 and -π/2 directions, value 0 represented the optic axis is on the center of the coordinate (0°). In DOPU parameter images, 1 indicated the single speckle light in tissues was fully polarized and 0 indicated complete depolarization. In different Stokes parameters, Q: Proportion of horizontally polarized light (Q=−1) or vertically polarized light (Q=+1); U: Proportion of light linearly polarized at 45° (U=−1) or linearly polarized at 135° (U=+1); V: Proportion of left-circularly polarized light (V=−1) or right-circularly polarized light (V=+1).

3. Results

3.1. Cross-sectional PS-OCT structure and tumor margin detection in different angles

To identify PS-OCT being able to detect the border of tumors within human kidneys, PS-OCT was used to obtain cross-sectional images with different angles (0° - 180° with 15° intervals) to distinguish normal and cancerous kidney tissues via polarization and Stokes parameters. Here, we showed representative cross-sectional PS-OCT images of normal and cancerous kidney tissues on the scanning angle of 0°, as shown in Fig. 3. In Fig. 3A-3G, we observed that normal kidney tissues were highly uniform in OCT intensity and polarization images. In contrast, tumor tissues were clustered and heterogeneous in intensity and polarization structures, as shown in Fig. 3H-3N. At the border of tumor tissue, polarization images showed obvious structure changes between normal and cancerous tissues (yellow and white window frames in Fig. 3H-3N), providing the accurate detection of tumor margins. We further zoomed in on the structure of tumor borders marked via yellow and white frames in Fig. 3H-3N. Although the OCT intensity image was able to approximately position the tumor region (Fig. 3H), the border of tumor tissues was still unclear (Fig. 3H_1 and 3H_2). Compared to the OCT intensity image, polarization images (retardation, optic axis, Stokes Q, and Stokes U) provided accurate detection of tumor borders with better contrast (yellow and white arrows in Fig. 3I_1, 3J_1, 3L_1, 3M_1 and Fig. 3I_2, 3J_2, 3L_2, 3M_2).

3.2. Enface PS-OCT structure and tumor profile detection in different depths

Since cross-sectional PS-OCT images were able to distinguish tumor borders and locate tumor regions, we employed 3D PS-OCT modes to obtain the volumetric structure of kidney tumors and sectioned *enface* images from different depths to show tumor profiles within human kidneys. In Fig. 4, we showed *enface* images of PS-OCT in intensity and polarization states at 245th, 305th, 405th, and 485th slices for tumor tissues and 305th slice for normal tissues. Similar to cross-sectional images, PS-OCT *enface* images showed that normal kidney tissues maintained highly uniform structures, as shown in Fig. 4A-4G. PS-OCT *enface* images of kidney tumor tissues (Fig. 4I-4N) in different depths indicated that tumor tissues were heterogeneous. The border and region of kidney tumors could be clearly differentiated based on the polarization changes. Particularly, PS-OCT images showed the specific distribution and profile of kidney tumor tissues. We marked the specific tumor tissue that showed significantly different polarization differences within kidney tumors (white arrows in retardation, blue arrows in optic axis, yellow arrows in DOPU, pink arrows in Stokes-Q, green arrows in Stokes-U, and red arrows in Stokes-V). These tumor tissues with different polarization states prominently distinguish tumor borders and locate tumor regions. Although kidney tumor regions were approximately located on intensity images (Fig. 4H), the borders between normal and tumor tissues were still challenging to identify compared to that in PS-OCT images. The precise border detection from PS-OCT was used to improve the accuracy of kidney tumor resection and minimize the unnecessary removal of normal kidney tissues.

3.3. PS-OCT structure and histology verification for tumor tissue distinguishment

PS-OCT provided the polarization information based on the birefringence of fibrosis tissues or collagens within human kidney tumors. To mark the tumor region out from the kidney tissue, we used the H&E histology as a gold standard to evaluate the accuracy of polarization states for extracting the polarization information of tumor tissues. Fig. 5A showed the H&E histology of the tumor tissue, which clearly showed the tumor region and border from normal kidney tissues. The tumor profile offered by the H&E histology was used to verify the results obtained from PS-OCT data. We calculated the probability distribution of polarization and Stokes parameter values from normal and cancerous tissues in Fig. 5H. The average between two adjacent peaks of probability distribution was set the threshold for distinguishing tumor areas from normal tissues (Fig. 5H). The polarization thresholds were 0.60, −0.55 & 0.69, 0.38, −0.35 & 0.45, −0.35 & 0.45, and −0.35 & 0.45 in retardation, optic axis, DOPU, Stokes-Q, Stokes-U, and Stokes-V parameters, respectively, as shown in Fig. 5B-G. These polarization thresholds effectively separated tumor regions from normal kidney tissues and achieved a good match with the tumor region provided by the histology. Moreover, we used the intrinsic optical attenuation coefficient to detect the kidney tumor region for comparing the accuracy of tumor detection by PS-OCT. As shown in Figure S1, the intensity profiles (Figure S1-C) along the axial scan lines in normal and tumorous OCT images (Figure S1-A and S1-B) showed significantly attenuated trends. The probability distribution of the attenuation coefficient (Figure S1-D) indicated that tumor tissues had two peaks and one peak overlaid with the peak of normal tissues. The mean value of the attenuation coefficient (2.04 mm^{-1}) between the peak probability in tumor (1.39 mm^{-1}) and normal (2.69 mm^{-1}) tissues was utilized to separate tumor tissues. Figure S1-E and S1-F showed the attenuation coefficient extracted images corresponding to Figure S1-A and S1-B. In Figure S1-H, we showed the *enface* structure of the tumor based on the attenuation coefficient. Compared to PS-OCT images, the attenuation coefficient could not match well with the histology (Figure S1-G).

Furthermore, we applied the Dice's coefficient to describe the degree of agreement between histology and PS-OCT data. Fig. 6 showed the process of calculating the degree of agreement between histology and PS-OCT data and the comparison between PS-OCT and the traditional attenuation contrast. We extracted tumor profiles (Fig. 6J-O) from the *enface* polarization images of retardation, optic axis, DOPU, Stokes-Q, Stokes-U, and Stokes-V parameters (Fig. 5B-G and Fig. 6B-G). Meanwhile, the tumor profile from the attenuation contrast image was also extracted (Fig. 6H and 6P), and the tumor profile from the H&E staining was labelled by the pathologist (Fig. 6A and 6I). Next, we overlaid the extracted H&E staining tumor profile and PS-OCT tumor profiles and the attenuation contrast tumor profile (Fig. 6Q-W). The Dice coefficient was calculated among each of the overlaid images. As shown in Table 1, we found that PS-OCT data presented good agreements with the histology (Dice's coefficient $>$ 0.86), while the attenuation coefficient method showed a smaller Dice score, which confirmed that PS-OCT offered better detection for kidney tumors. With polarization images, we observed that tumor borders were particularly highlighted in the imaging of optic axis, Stokes-U, and Stokes-V parameters (white arrows), indicating that kidney tumor borders primarily induced more changes in optic axis, 45°/135° linearly polarized light, and the circularly polarized states. Moreover, tumor regions were mainly highlighted via retardation, Stokes-U, and Stokes-V, which presented that tumor tissues induced the primary change of phase delays, 45°/135° linearly polarized light, and the circularly polarized states. DOPU primarily quantified the tumor region but lacked the quantification of tumor borders. The followed separation and differentiation of tumor borders and regions were based on the same polarization and Stokes thresholds.

We further validated the thresholds by evaluating the difference in various polarizations between normal and tumorous tissues. Five regions were selected from each 2D cross-sectional PS-OCT frame in 30 normal and tumor samples for the data statistics. In Fig. 7A-7N, the attenuation coefficient (Fig. 7A and 7H) and PS-OCT data showed that normal tissues had a high uniformity, but tumor tissues displayed a high heterogeneity. Fig. 7O-7U showed the statistical plots corresponding to the attenuation coefficient, polarization, and Stokes parameters to describe the difference of tissue values in normal and tumorous kidneys. Although the attenuation coefficient between normal and tumor tissues showed a significant difference, the difference in the probability of the tissue changing degree was not as obvious as in PS-OCT data. Within the

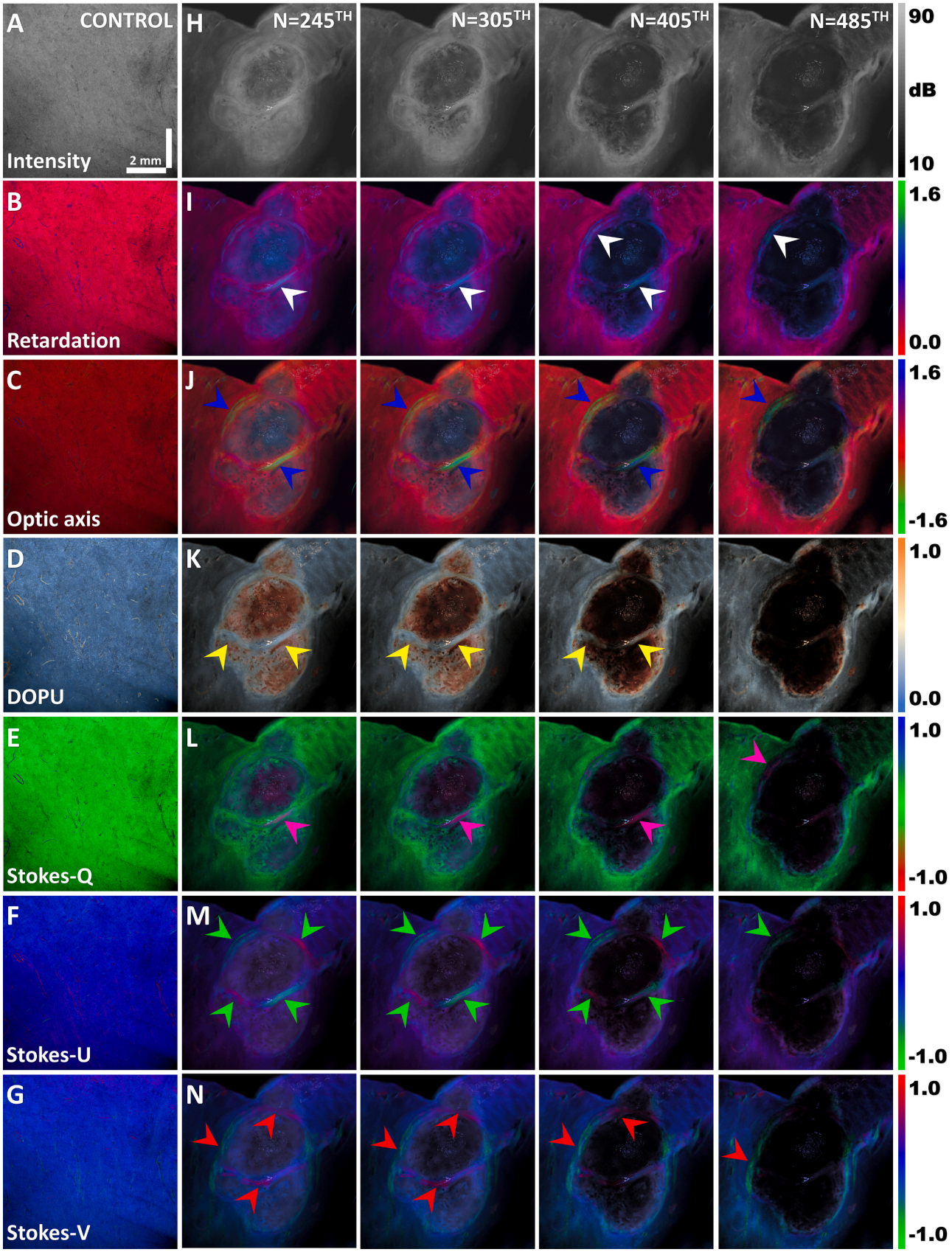

Fig. 4. Representative *enface* projection PS-OCT images of kidney normal and tumor tissues in different depths. A-G, *enface* PS-OCT images of kidney normal tissues at 305th slice. H—N, enface PS-OCT images of kidney tumor tissues at 245th, 305th, 405th, and 485th slices.

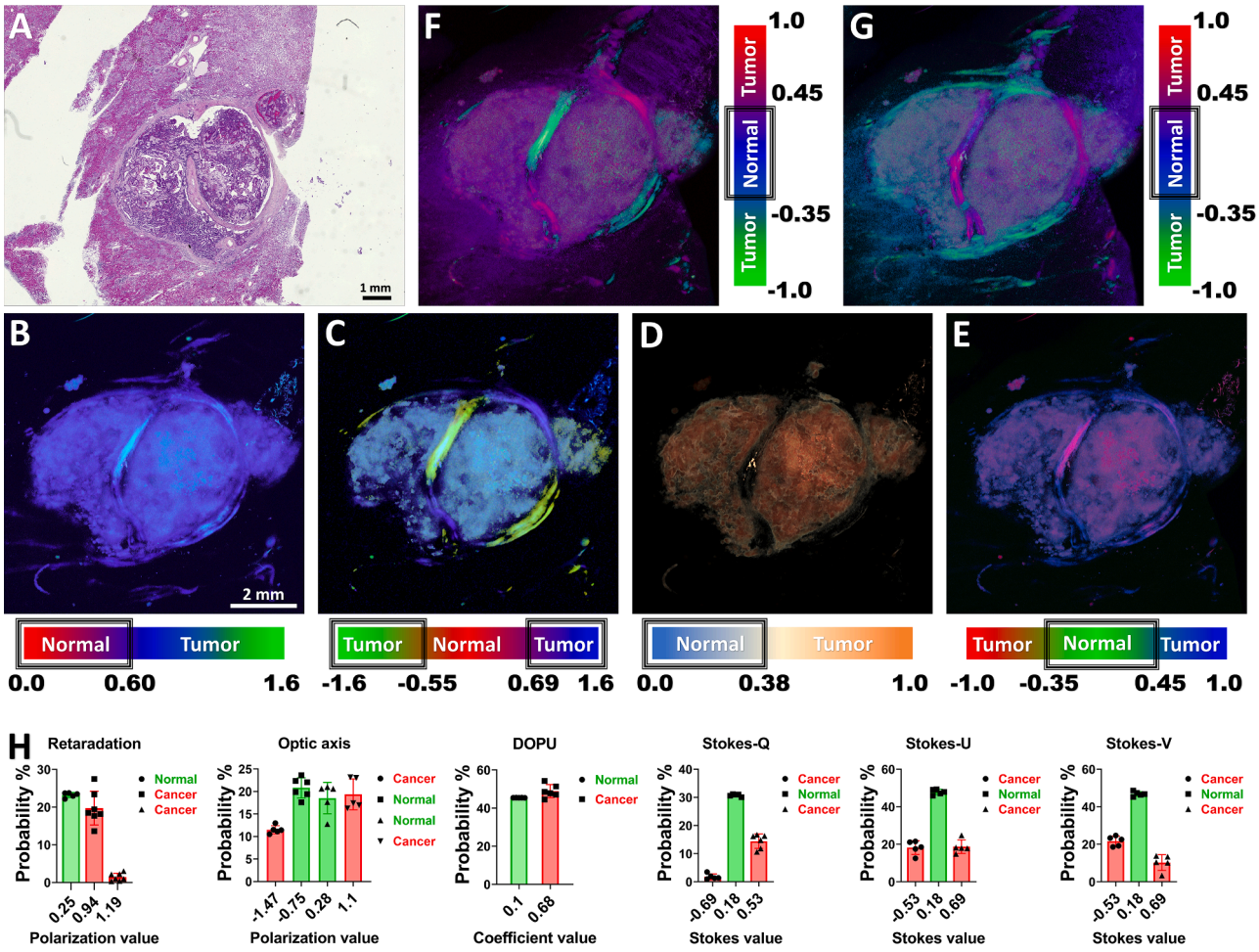

Fig. 5. *Enface* histology and PS-OCT images of tumor region extraction in human kidney tumor samples. A, H&E histology of the kidney tumor sample. B-G, extracted *enface* polarization images of retardation, optic axis, DOPU, Stokes-Q, Stokes-U, and Stokes-V parameters based on the thresholds. H, Statistic histogram of the probability distribution of polarization and Stokes parameter values for normal and cancer tissues. Color-bars and values corresponded to the polarization state range of the corresponding polarization and Stokes parameter values. Dark frames on color-bars represented the threshold of the corresponding polarization parameter for distinguishing tumor and normal tissues. The corresponding polarization state ranges separated by the threshold were labeled the corresponding normal and tumor tissues. Sample size, $N = 6$.

comparison of polarization parameters, Stokes-U and Stokes-V parameters had a lower probability of the degree of tissue changing in kidney tumors. This result indicated that the efficacy of using PS-OCT data to distinguish tumor tissues was higher than the attenuation coefficient.

Based on the validated thresholds, we further extracted the tumor borders from cross-sectional polarization images, as shown in Fig. 8. We zoomed in on the sub-figures cropped from the two sides of tumor tissues in OCT intensity and PS-OCT polarization images. In Fig. 8B_1-8G_1 and 8B_2-8G_2, we clearly observed that tumor borders were differentiated by the polarization differences that were marked by different colors in polarization and Stokes parameters, which was unable to be directly differentiated in the OCT intensity images (Fig. 8A, 8A_1, and 8A_2). After applying the thresholds, we extracted the tissue structure with different polarization changes at the tumor border, as shown in Fig. 8$B_{1\text{-}2}$-6$G_{1\text{-}2}$ and 8$B_{2\text{-}2}$-6$G_{2\text{-}2}$. Polarization-extracted PS-OCT images could precisely locate tumor regions within the human kidney.

3.4. 3D PS-OCT structure and tumor tissue distinguishment

To show the spatial structure of the kidney tumor, we further provided the 3D PS-OCT intensity and polarization images. Fig. 9A showed the 3D intensity structure of the kidney tumor but the tumor border was not clear. The intensity difference on the surface may be caused by the uneven structure of the surface. Based on the polarization thresholds, we separated the 3D tumor region from kidney normal tissues, as shown in Fig. 9B-G. We observed that different polarization parameters marked the main tumor regions and borders and highlighted different tissue distribution within the spatial structure of the tumor. The 3D polarization structure of the kidney tumor from Stokes parameters showed the degree of changes in different polarization states (linear, circular, and elliptical). Fig. 9B_1-G_1 showed the complete 3D polarization structure of the kidney tumor including kidney tumor and normal tissues. With the 3D tumor structure overlaid images between polarization and intensity images (Fig. 9B_2-G_2), tumor borders and regions could be clearly distinguished and positioned from normal kidney tissues.

To further display the tumor region and border in different depths within the human kidney, we showed the overlaid polarization and intensity images of the tumor at different depths. Fig. 9H-M showed the slice structure of the tumor at 245th, 305th, 405th, and 485th depths in 3D PS-OCT polarization images. At different depths, tumor tissues showed different tumorous regions and borders. Fig. 9H_1_M_1 showed the overlaid tumor structure with the 3D polarization images and intensity images at the same depths. To clearly show the tumor region and border from overlaid images at different depths, we further displayed the overlaid *enface* polarization tumor tissue structures with the axial-projection *enface* OCT intensity structures at the corresponding depths.

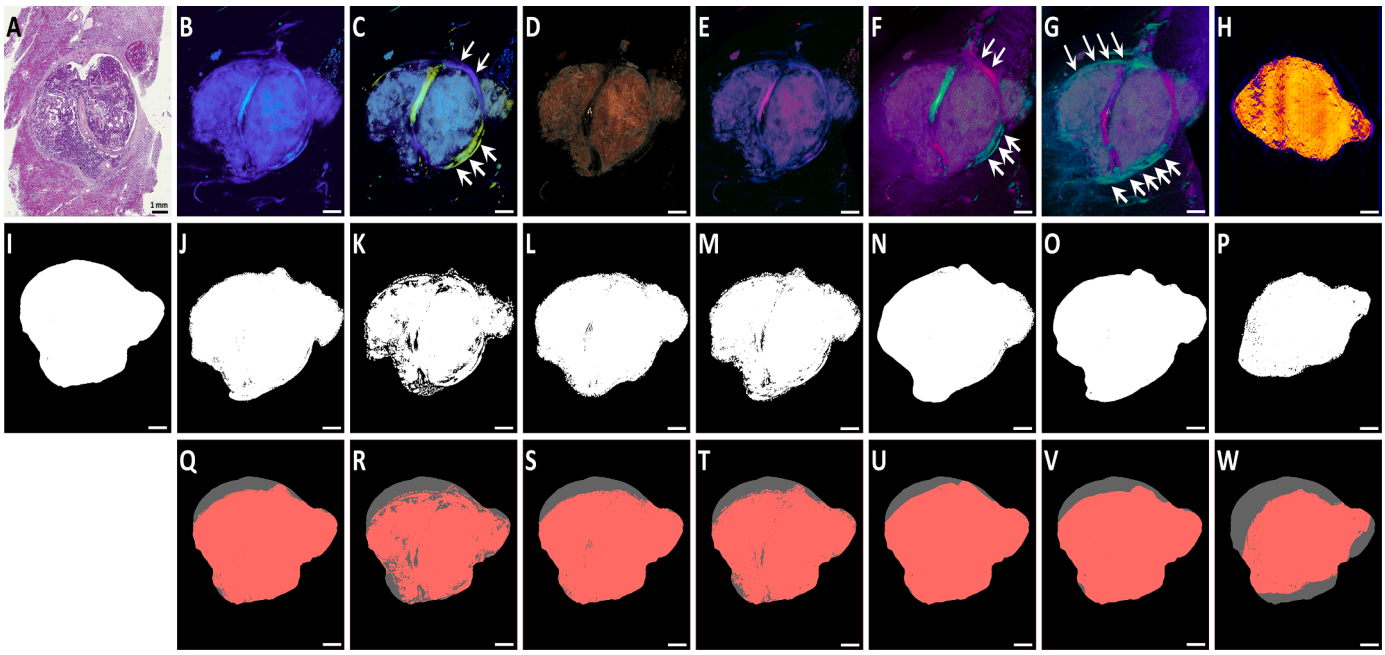

Fig. 6. Comparison of the degree of agreement between H&E staining and polarization-extracted PS-OCT images. A, H&E staining histology. B-G, polarization-extracted images of retardation, optic axis, DOPU, Stokes-Q, Stokes-U, and Stokes-V parameters. H, the intrinsic optical attenuation contrast. I, the labelled tumor profile from H&E staining by the pathologist. J-P, extracted tumor profiles from retardation, optic axis, DOPU, Stokes-Q, Stokes-U, Stokes-V, and attenuation contrast parameters. Q-W, the overlaid images between the extracted H&E staining tumor profile and PS-OCT parameters and the attenuation contrast.

Table 1
Dice's coefficient of tumor regions at the matching between PS-OCT (retardation, optic axis, DOPU, Stokes-Q, Stokes-U, Stokes-V, and attenuation coefficient) and the histology.

	Retardation	Optic axis	DOPU	Stokes-Q	Stokes-U	Stokes-V	Attenuation
Histology	0.886	0.867	0.889	0.886	0.890	0.880	0.802

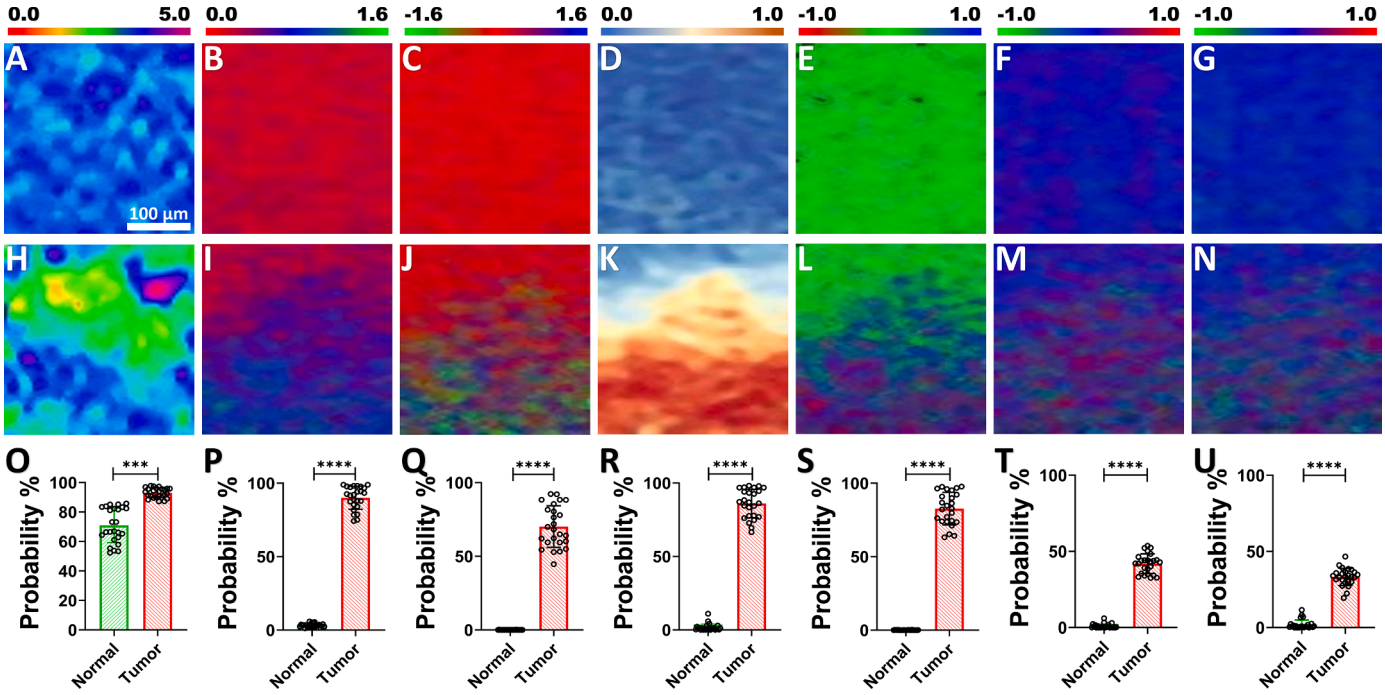

Fig. 7. Statistical plots in the probability of the degree of the tissue changing in normal and tumor tissues. A-G, attenuation coefficient, retardation, optic axis, DOPU, Stokes-Q, Stokes-U, and Stokes-V in normal tissues. H—N, attenuation coefficient, retardation, optic axis, DOPU, Stokes-Q, Stokes-U, and Stokes-V in tumor tissues. O-U, corresponding statistical histograms of attenuation coefficient, retardation, optic axis, DOPU, Stokes-Q, Stokes-U, and Stokes-V in normal and tumor tissues. Significant value: ***, $p < 0.001$. ****, $p < 0.0001$. $N = 6$.

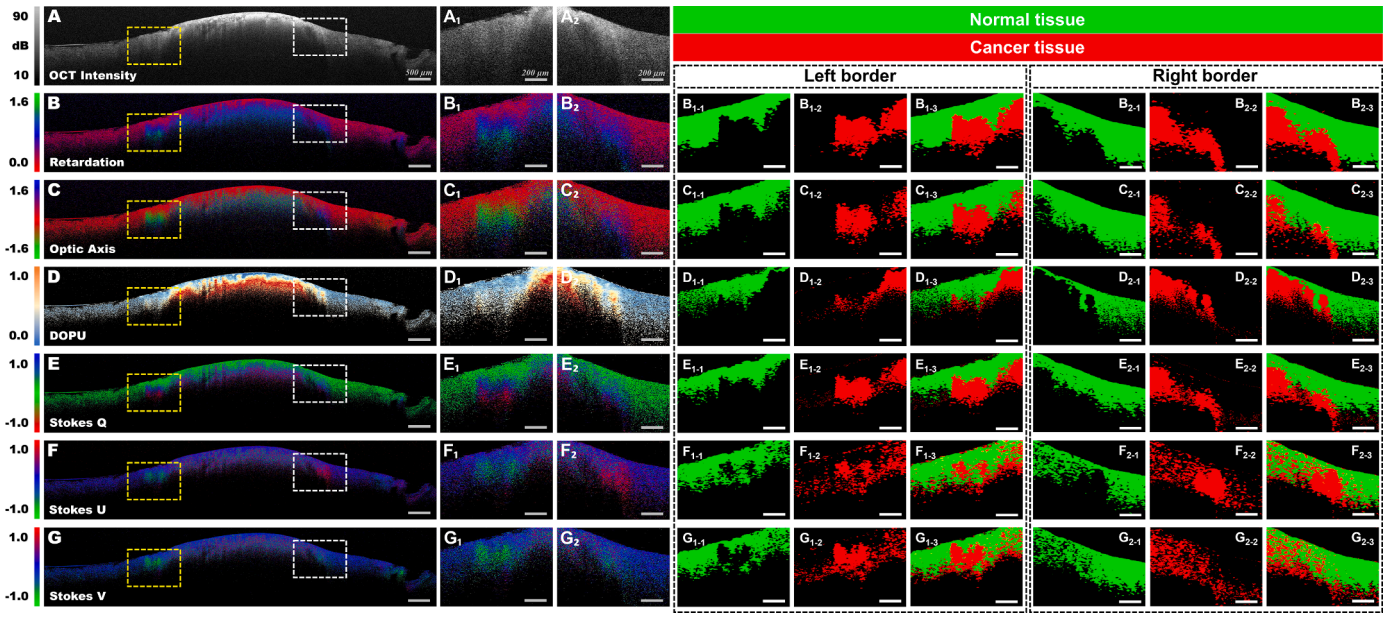

Fig. 8. Representative cross-sectional polarization-extracted PS-OCT images and OCT intensity based on histology verification at tumor borders. A-G, cross-sectional tumor images in OCT intensity, retardation, optic axis, DOPU, Stokes-Q, Stokes-U, and Stokes-V parameters. A_1-G_1, left tumor border images in OCT intensity, retardation, optic axis, DOPU, Stokes-Q, Stokes-U, and Stokes-V parameters. A_2-G_2, right tumor border images in OCT intensity, retardation, optic axis, DOPU, Stokes-Q, Stokes-U, and Stokes-V parameters. $B_{1-1,2,3}$-$G_{1-1,2,3}$, polarization-extracted left tumor border images in OCT intensity, retardation, optic axis, DOPU, Stokes-Q, Stokes-U, and Stokes-V parameters. $B_{2-1,2,3}$-$G_{2-1,2,3}$, polarization-extracted right tumor border images in OCT intensity, retardation, optic axis, DOPU, Stokes-Q, Stokes-U, and Stokes-V parameters.

From these overlaid *enface* images, we observed that polarization and Stokes parameters from PS-OCT data not only displayed the tumor border and region at different depths but also provided the information on tissue distribution within the tumor via the polarization difference. Particularly, the tumor border (red arrows in retardation, yellow arrows in optic axis, green arrows in Stokes-Q, blue arrows in Stokes-U, and white arrows in Stokes-V, Fig. 9H_2, 9I_2, 9K_2-L_2) was highlighted at different depths based on the different sensitive degree to polarization and Stokes parameters, which could be effective to guide doctors to precisely position tumor regions from normal tissues during the surgery.

Fig. 10 showed the comparison of the tumor region among polarization states and Stokes parameters at different depths. With these zoomed in structures of tumor tissues, we observed that different polarization and Stokes parameters revealed different tissue structures within the kidney tumor. At the same depth, DOPU (Fig. 10C—C_1—C_2, 10I-I_1-I_2, 10O—O_1—O_2, and 10U-U_1-U_2) mainly highlighted tumor tissues but did not show internal tumor borders. Compared to retardation, optic axis, Stokes-Q, Stokes-U, and Stokes-V in Fig. 10M_2, 10N_2, 10P_2, 10Q_2, and 10R_2, DOPU (Fig. 10O_2) were unable to distinguish the internal tumor margin tissues. Moreover, polarization images (retardation, optic axis, and DOPU) did not show the same tumor profiles from sub-figures at different depths. Meanwhile, Stokes parameters also showed the ununiformed tissue distributions and borders within the tumor. These differences in polarization and parameters indicated that the polarization images could be used to precisely locate and distinguish kidney tumor regions and borders in a complementary manner.

4. Discussion

The regular treatment for kidney tumors was surgical resection which required completely removing cancerous tissues to avoid recurrence and maximumly keeping normal tissues. Therefore, accurate identification of the tumor region and boundary played an impactful role in the surgical removal of kidney tumors. Although many conventional imaging systems such as CT, MRI, and ultrasonography could provide large FOV for tumor diagnosis, the low spatial resolution prohibited the surgery from precisely resecting tumorous tissues from surrounding normal tissues. Moreover, CT and MRI faced the challenge of providing imaging guidance during the surgery in real-time which was one of the most critical parts of clinical surgical removals. OCT had been demonstrated as a promising tool to distinguish normal and cancerous tissues in brain, kidney, oral, and skin tumors [19,34-36]. However, the intensity-based OCT structure images lacked tissue-specific contrast, which resulted in limited differentiation of the boundary between normal and cancerous tissues to further map the profile of tumors for complete surgical removal. Particularly, the border between normal and cancerous tissues consists of partial tumorous and normal tissues, as well as transferring and degenerating tissues, which was difficult to induce enough change of structure and tissue formation that could be detected by current imaging modalities.

In this study, we demonstrated that PS-OCT was able to accurately detect tumor-associated fibrosis and distinguish tumorous tissues from normal tissues based on tissue birefringence. Compared to intensity-OCT in both cross-sectional and *enface* images, our results indicated that polarization parameters of retardation, optic axis, and DOPU, as well as Stokes parameters of Q, U, and V, provided a more precise boundary differentiation between tumorous and normal tissues. The existed tubules/lesions within the kidney (Fig. 3H and 3H_1, white frame) caused confusion for distinguishing the border in OCT intensity images, while PS-OCT images (Fig. 3I-N and 3I_2—N_2) could precisely locate the boundary between cancerous and normal tissues (Figure 3I_{ii}-N_{ii}). The *enface* structure of OCT intensity images was able to map the profile of the tumor region, however, the precise differentiation of the border between tumorous and normal tissues could only be detected by PS-OCT images based on the tissue birefringence, especially PS-OCT optic axis, Stokes-U, and Stokes-V images, as shown in Fig. 4J, 4M, and 4N (blue, green, and red arrows). The capability of precise differentiation of tumorous tissue from normal adjacent tissues by PS-OCT could be taken advantage of to accurately find the tumor border in the mixed field of non-adequate tumorous, normal, and degenerative tissues in clinical renal cancer removal surgeries. This technique could maximumly retain the normal kidney tissue for essential human physiological function and

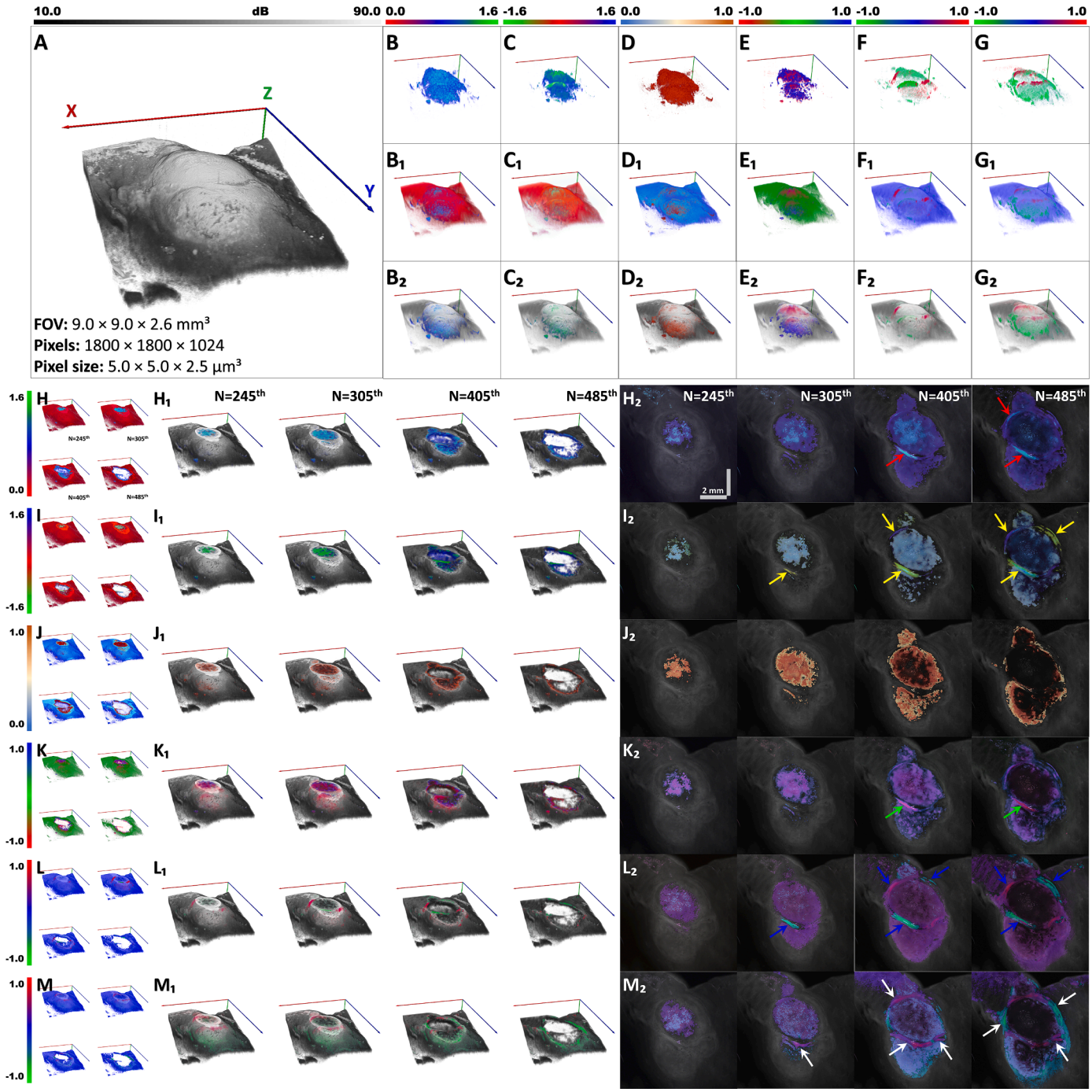

Fig. 9. 3D and slice diagrams of OCT intensity and polarization of tumor regions and borders at different depths for human kidney tumors. A, 3D intensity-based OCT image of the kidney tumor. B-G, polarization-extracted 3D structures of the kidney tumor in retardation, optic axis, DOPU, Stokes-Q, Stokes-U, and Stokes-V parameters. B_1-G_1, 3D complete polarization images including the kidney tumor and normal tissues in retardation, optic axis, DOPU, Stokes-Q, Stokes-U, and Stokes-V parameters. B_2-G_2, 3D overlaid images between the polarization and the OCT intensity-based structure. H-M, slice diagrams of 3D polarization images in retardation, optic axis, DOPU, Stokes-Q, Stokes-U, and Stokes-V parameters. H_1_M_1, slice diagrams of 3D overlaid images between the polarization and the intensity images in retardation, optic axis, DOPU, Stokes-Q, Stokes-U, and Stokes-V parameters at different depths. H_2_M_2, 2D *enface* overlaid images between the polarization and the intensity images in retardation, optic axis, DOPU, Stokes-Q, Stokes-U, and Stokes-V parameters. Depth slices were at 245th, 305th, 405th, and 485th, respectively.

metabolism and completely resect the tumor tissue. In terms of imaging speed for clinical translation, the acquisition time of each B-scan for single channel is ~6 ms for our OCT system with an A-Scan rate of 48 KHz, which is consistent with the imaging speed for guiding mouse brain tumor removal in a previous study [37]. The image acquisition time of each frame in clinical ophthalmology surgeries is ~ 9–15 ms [38,39], thus our image acquisition speed is comparable with those reported in the clinical studies. However, it takes 75.814 s to obtain seven 9 × 9 × 2.6 mm^3 (1800 × 1800 × 1024 pixels) 3D images (including intensity, retardation, optic axis, DOPU, Stokes-Q, Stokes-U, Stokes-V). With the recently reported ultrafast OCT laser design up to MHz [40], the ultrahigh-speed 3D OCT image acquisition can reach multi-cm^3 fields per second in the future study.

In the study of quantitative distinguishing tumors from surrounding normal tissues, the intrinsic optical attenuation coefficient has been widely applied to detect tumor regions [20,35,41]. There was a

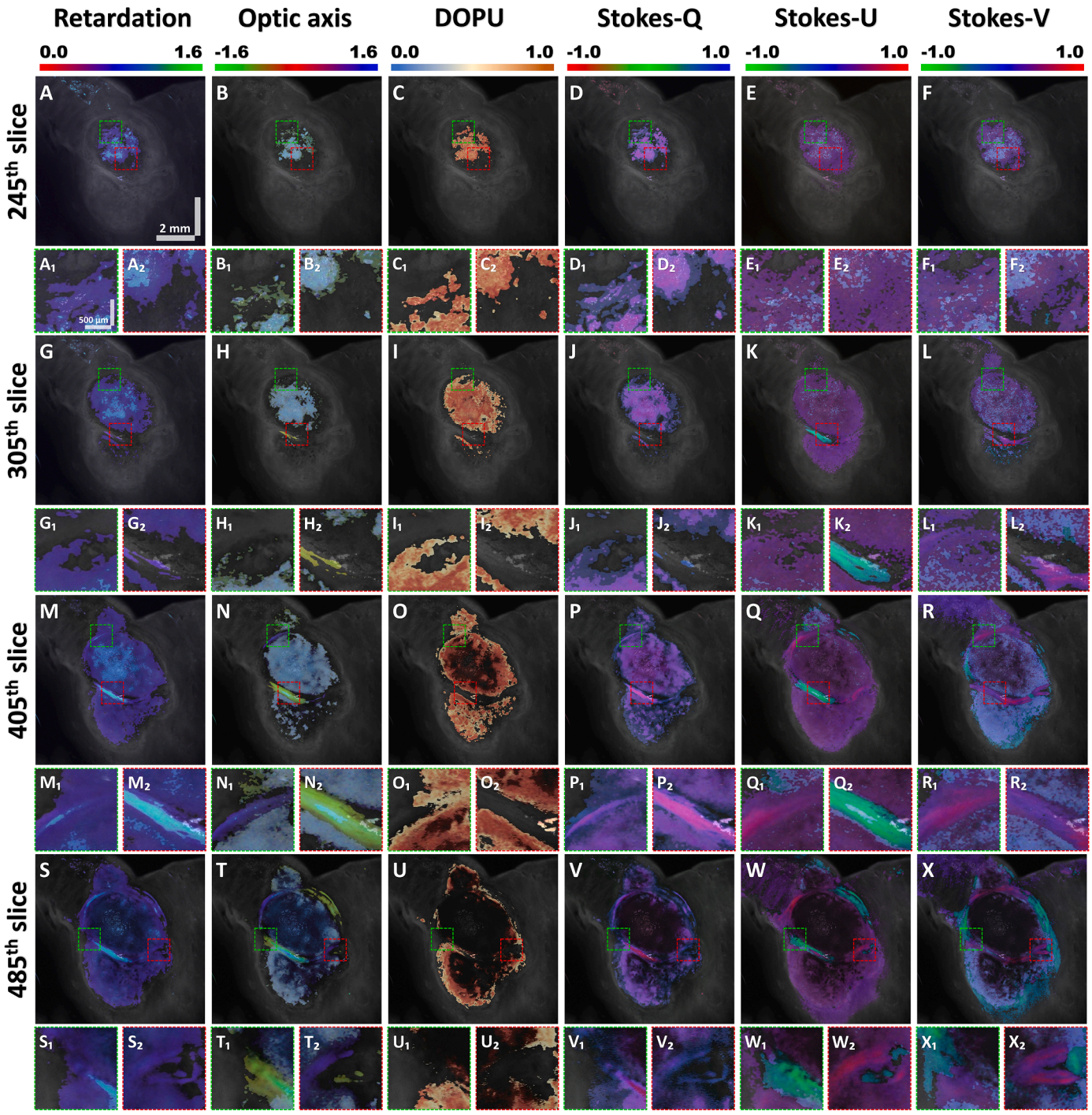

Fig. 10. Comparison of tumor regions among polarization states and Stokes parameters at different depths. A-F, tumor regions in different polarization and Stokes parameters at 245th slice. G-L, tumor regions in different polarization and Stokes parameters at 305th slice. M-R, tumor regions in different polarization and Stokes parameters at 405th slice. S-X, tumor regions in different polarization and Stokes parameters at 485th slice. A_1-X_1 and A_2-X_2 were zoomed in sub-figures corresponding to the green (A_1-X_1) and red (A_2-X_2) frames in A-X at 245th, 305th, 405th, and 485th slices.

significant difference in the attenuation coefficient between cancerous and normal renal tissues [35,42,43], which was employed to distinguish tumor regions from normal kidney tissues. We calculated the attenuation coefficient in tumorous and normal tissues and found that tumor tissues had a smaller attenuation coefficient than that of normal tissues, as shown in Figure S1D. Our results were consistent with that reported in [40] that tumor tissues had a smaller attenuation coefficient, while we also noticed there were studies in [36] and [39] indicated that tumor tissues had a larger attenuation coefficient compared to normal renal tissues. Therefore, the application of the attenuation coefficient for differentiating kidney tumor boundary still faced the limitation because of the difference of renal tumors in different patients. In this study, we used polarization parameters (retardation, optic axis, and DOPU) and Stokes parameters (Q, U, and V) to make a comparison with the attenuation coefficient via the Dice coefficient and the histology verification. We found that PS-OCT images provided a higher agreement of the tumor region detection with the histology than the attenuation coefficient method (Table 1). The attenuation coefficient could roughly detect the main tumor region, but the tumor boundary information was missed. In contrast, Fig. 6 showed that PS-OCT detections effectively located the

border between tumorous and normal tissues which was highly consistent with the histology. Thus, our results confirmed that PS-OCT was able to offer more accurate and consistent detection of kidney tumor boundary compared to the attenuation coefficient.

In addition to distinguishing tumor regions from normal tissues, PS-OCT also provided the 3D information of tumors to create the volumetric structure visualization in real-time for surgical guidance. 3D spatial visualization showed significant advantages in tumor localization compared to standard 2D slice visualization for surgical guidance [44, 45]. The 3D structure of kidney tumors from PS-OCT scanning allowed multi-parameter spatial distinguishment from normal tissues, which was significantly more accurate than that of traditional intensity-based OCT structures. 3D polarization parameter visualizations directly located tumor borders and zones in spatial structures that could clearly guide surgeons to resect tumors or check the effect of surgical resection. Moreover, given the constrained depth of penetration inherent to PSOCT, its application in clinical settings to guide the excision of kidney tumors along the interface between healthy and tumorous tissues necessitates a sequential approach. Given that tumor resection by surgeons entails a multi-step process rather than a single-cut procedure, PSOCT can serve as a valuable tool for progressively identifying the resection area. This involves conducting imaging after each successive resection, thereby facilitating a step-by-step approach towards achieving complete tumor removal. PS-OCT was also capable to visualize the distribution of fibrosis and tumor tissues within kidneys, which provided further benefits for guiding tumor samplings *in vivo* in clinical medical research. The visualization of the internal distribution of tumorous tissues based on PS-OCT could assist surgeons to acquire the most representative tumorous tissues, which was critical to conducting oncology clinical assays and gene sequencing. Molecular and genetic analysis of the tumor tissue in patients was significant for anti-metastasis and anti-recurrence therapies, which was also crucial for post-surgery drug screening and therapy [46–48]. Therefore, our results demonstrated that PS-OCT had the potential to play a key role in the guidance of the tumor sampling and assay of renal cancer. This study also provided the quantitative evaluation of tumorous renal tissue from retardation, optic axis, DOPU, Stokes-Q, Stokes-U, and Stokes-V parameters to demonstrate the availability of PS-OCT in the precise detection of kidney tumor boundary. Although the intrinsic optical attenuation contrast of kidney tumors showed there was a significant difference between tumor and normal tissues (Fig. 7O), the difference of tissues from kidney tumors and normal tissues was not as obvious as in PS-OCT parameters (Fig. 7P-U). Tubules, arterioles, and fibrosis within kidneys were also able to cause the same attenuation contrast as tumorous tissues [49,50], Figure S1E showed that there were still low attenuation coefficient tissues within normal kidney samples, which might cause relative larger errors to distinguish tumor borders. In contrast to the attenuation contrast, PS-OCT polarization parameters had more significant differences between tumorous and normal kidney tissues. The classification probability of PS-OCT parameters for normal samples was close to 0 which was significantly different from tumorous samples. This character indicated that PS-OCT has obvious advantages in the kidney tumor border distinguishment compared to the attenuation contrast. However, larger-scale studies need to be performed in the future to further validate the findings of this study prior to clinical surgeries.

PS-OCT also provided the visualization of internal tissue distributions within kidney tumor including microstructures and tissue categories. Based on the H&E staining, we found that the tumor is circumscribed with prominent fibrous pseudocapule (black arrows in Figure S2A). There are cavity areas (cyan arrows in Fig. 11A) and papillary structures (black arrows in Fig. 11B) existed in RCCs. Therefore, we could suggest that the tumor type was probably a papillary RCCs because tumor cells form many papillary structures that have a fibrovascular core (representatively indicated by orange arrows in

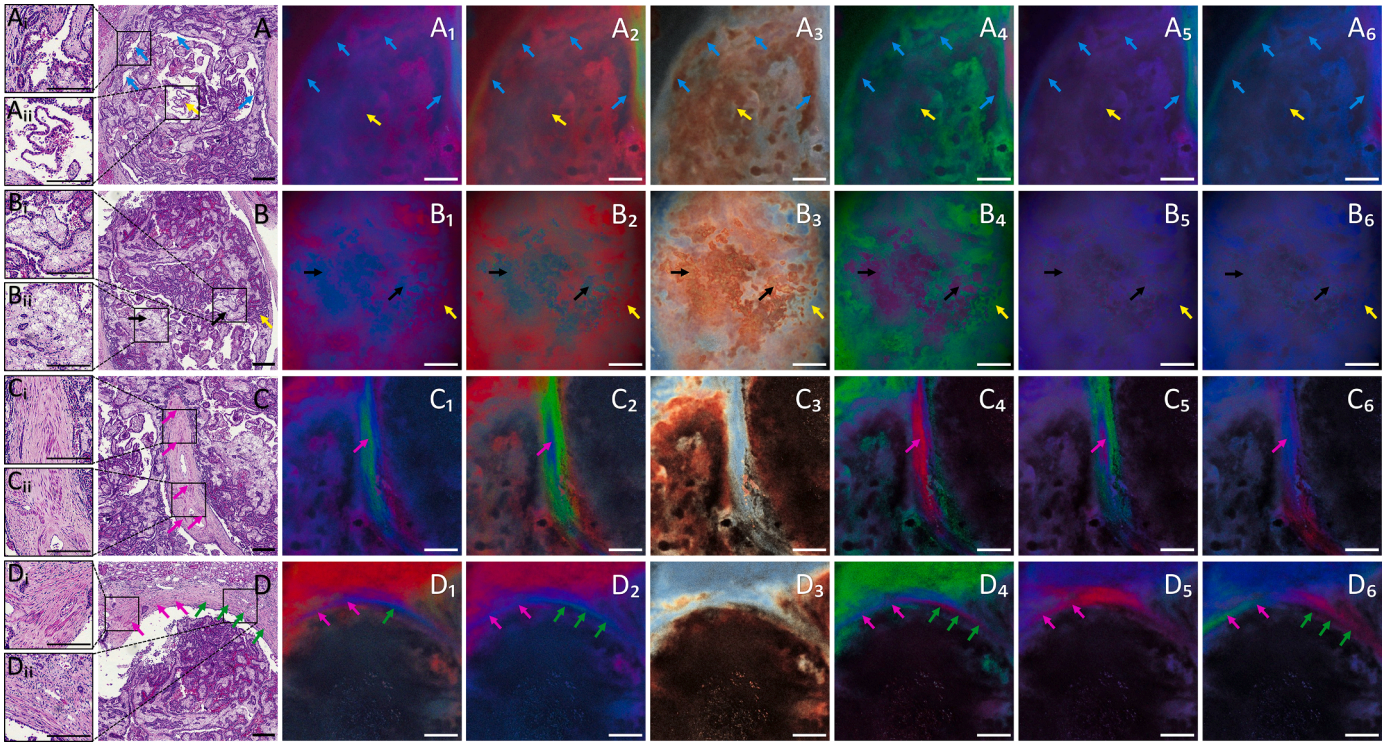

Fig. 11. Comparison of the recognition of tumor internal microstructures between H&E staining and PS-OCT images. A-D, representative H&E staining of internal tissues and borders of kidney tumors. A_i-D_i and A_{ii}-D_{ii}, enlarged microstructures corresponded to representative histology images. A_1-A_6, B_1-B_6, C_1–C_6, and D_1-D_6, parameter images of retardation, optic axis, DOPU, Stokes-Q, Stokes-U, and Stokes-V from PS-OCT corresponding to representative H&E staining. Cyan arrow, cavity, or empty area. Yellow arrow, tumor cells. Black arrow, papillary structures. Pink arrow, smooth muscles. Green arrow, myofibroblasts on the fibrous pseudocapsule. Scale bar is 350 μm.

Figure S2B and black circle in Figure S2C) and surrounded by a layer of cuboidal or columnar tumor cells [51,52]. We could also observe the same cavity areas (cyan arrows) and papillary structures (black arrows) from the corresponding PS-OCT images as shown in Fig. 11$A_{1\text{-}6}$ and $B_{1\text{–}6}$. This indicated that PS-OCT was able to detect kidney tumor microstructures for further distinguishing tumor types. It also matched the different tissue structures that we observed at different depths within the tumor (Fig. 10). Moreover, H&E staining allowed us to observe the tumor borders compromised by fibrous tissue, smooth muscle fibers (pink arrows in Fig. 11C and D, yellow arrows in Figure S2D, E, and F), and myofibroblasts (green arrows in Fig. 11D, Red arrows in Figure S2D and E). We found that the corresponding PS-OCT images (Fig. 11$C_{1\text{-}6}$ and $D_{1\text{–}6}$) showed the same components of smooth muscle fibers (pink arrows) and myofibroblasts (green arrows). By the existence of the papillary edema (Figure S2C and D), foamy macrophages (Figure 11B_i and B_{ii}) in papillary cores, and a thick fibrous capsule (Fig. 11C and D, Figure S2A, D, and F), we suggested that the tumor subtype belonged to Type-1 papillary RCCs [52,53]. In PS-OCT data, we clearly observed critical structures and components provided by H&E staining which was employed to clarify the type of kidney tumors clinically. This result demonstrated that PS-OCT had the potential to provide a clinical classification of RCCs based on the detection of the internal microstructure and tissue distribution of tumors. Compared to histology, PS-OCT had the advantage of real-time imaging and *in vivo* scanning to save time for diagnosis and treatment planning. Additionally, we found that PS-OCT polarization and Stokes parameters had different sensitiveness to different microstructures and tissues, which could be used for the characterized analysis of the specific type of RCCs and longitudinal tracking of therapeutic effects such as chemotherapy and radiotherapy.

One limitation to notice is that the PS-OCT system in this study is based on single input polarization state, thus the polarization parameters (phase retardation, optic axis, and DOPU) are all cumulative values [54]. The cumulative phase retardation only indicates the phase retardation between the principal polarization states along the complete optical path through the tissue rather than the phase retardation effect at a single depth location [55,56]. Therefore, the 'local' polarization information was not able to be quantitatively provided. One the other hand, since the local birefringence mode was proportional to the amount of the actual birefringent signal per pixel in the OCT images, the local polarization signal suffers from a lower sensitivity [57,58]. Compared to the local polarization state, the cumulative polarization mode provided higher sensitivity and required much simpler system, therefore was always preferred for binary decisions [55,58,59]. Considering the key to the surgical guidance for renal tumor resection is the differentiation between normal and cancerous tissues to avoid residual tumor tissues, we hereby applied the cumulative polarization parameters to detect tumor margins and regions.

Conclusion

The structure and polarization information provided by PS-OCT was shown to offer a significant improvement in contrast between renal cancer and normal kidney tissues. PS-OCT polarization parameters provided depth-resolved, cross-sectional, and spatial structure information to achieve real-time distinguishment of kidney tumor borders and regions. We demonstrated that PS-OCT imaging could achieve more accurate detection and differentiation of tumor margins and zones compared to the intrinsic optical attenuation contrast. The results indicate that PC—OCT was able to visualize the tissue distribution of kidney tumor for assisting tumor sampling and surgical guidance. The result of our study provides important information for translating PS-OCT to *in vivo* clinically surgical resection guidance in the future.

Funding

This work was supported by grants from the University of Oklahoma Health Sciences Center (3P30CA225520), Institutional Research Grant number IRG-19-142-01 from the American Cancer Society, National Science Foundation (OIA-2132161, 2238648), National Institute of Health (R01DK133717), Oklahoma Shared Clinical and Translational Resources (NIGMS U54GM104938), Oklahoma Center for the Advancement of Science and Technology (HR23-071), and the medical imaging COBRE (P20GM135009). Histology service provided by the Tissue Pathology Shared Resource was supported in part by the National Institute of General Medical Sciences COBRE Grant P20GM103639 and National Cancer Institute Grant P30CA225520 of the National Institutes of Health. Financial support was provided by the OU Libraries' Open Access Fund.

CRediT authorship contribution statement

Feng Yan: Conceptualization, Methodology, Software, Formal analysis, Investigation, Data curation, Writing – original draft. **Chen Wang:** Formal analysis, Investigation. **Yuyang Yan:** Formal analysis, Investigation. **Qinghao Zhang:** Formal analysis, Investigation. **Zhongxin Yu:** Validation, Writing – review & editing. **Sanjay G. Patel:** Validation, Writing – review & editing. **Kar-Ming Fung:** Validation, Resources, Writing – review & editing. **Qinggong Tang:** Conceptualization, Validation, Resources, Data curation, Writing – review & editing, Supervision, Project administration, Funding acquisition.

Declaration of Competing Interest

The authors declare that they have no known competing financial interests or personal relationships that could have appeared to influence the work reported in this paper.

Data availability

Data will be made available on request.

Acknowledgment

The authors are grateful to Trisha I. Valerio, Coline Furrer, Sophie X. Patrock, and Jacob P. Adams for providing language help and grammar assistance in this article.

Supplementary materials

Supplementary material associated with this article can be found, in the online version, at doi:10.1016/j.optlaseng.2023.107900.

References

[1] Chow W-H, Dong LM, Devesa SS. Epidemiology and risk factors for kidney cancer. Nat Rev Urol 2010;7:245–57.
[2] Capitanio U, Montorsi F. Renal cancer. Lancet North Am Ed 2016;387:894–906.
[3] Yong C, Stewart GD, Frezza C. Oncometabolites in renal cancer. Nat Rev Nephrol 2020;16:156–72.
[4] Padala SA, Barsouk A, Thandra KC, Saginala K, Mohammed A, Vakiti A, Rawla P, Barsouk A. Epidemiology of renal cell carcinoma. World J Oncol 2020;11:79.
[5] Zieren RC, Dong L, Pierorazio PM, Pienta KJ, de Reijke TM, Amend SR. Extracellular vesicle isolation from human renal cancer tissue. Med Oncol 2020;37:1–11.
[6] Patel HD, Semerjian A, Gupta M, Pavlovich CP, Johnson MH, Gorin MA, Allaf ME, Pierorazio PM. Surgical removal of renal tumors with low metastatic potential based on clinical radiographic size: a systematic review of the literature, urologic oncology: seminars and original investigations. Elsevier; 2019. p. 519–24.
[7] Porta C, Cosmai L, Leibovich BC, Powles T, Gallieni M, Bex A. The adjuvant treatment of kidney cancer: a multidisciplinary outlook. Nat Rev Nephrol 2019;15:423–33.
[8] Krajewski KM, Pedrosa I. Imaging advances in the management of kidney cancer. J Clin Oncol 2018;36:3582.
[9] Auberton E, Bellin M, Richard F, Chatelain C, Delcourt A, Grellet J. Comparative study of MRI and CT x-ray in evaluating the extension of kidney cancer in adults. J Radiol 1989;70:327–36.

[10] Helenon O, Denys A, Chretien Y, Souissi M, Melki P, Cornud F, Dufour B, Moreau J. Role of MRI in the diagnosis of kidney cancer. J Radiol 1993;74:105–15.
[11] Wake N, Wysock JS, Bjurlin MA, Chandarana H, Huang WC. Pin the tumor on the kidney:" an evaluation of how surgeons translate CT and MRI data to 3D models. Urology 2019;131:255–61.
[12] Margreiter M, Marberger M. Focal therapy and imaging in prostate and kidney cancer: high-intensity focused ultrasound ablation of small renal tumors. J Endourol 2010;24:745–8.
[13] Hsiao Y-H, Kuo S-J, Tsai H-D, Chou M-C, Yeh G-P. Clinical application of high-intensity focused ultrasound in cancer therapy. J Cancer 2016;7:225.
[14] Rossi SH, Klatte T, Usher-Smith JA, Fife K, Welsh SJ, Dabestani S, Bex A, Nicol D, Nathan P, Stewart GD. A decision analysis evaluating screening for kidney cancer using focused renal ultrasound. Eur Urol Focus 2021;7:407–19.
[15] Christensen-Jeffries K, Couture O, Dayton PA, Eldar YC, Hynynen K, Kiessling F, O'Reilly M, Pinton GF, Schmitz G, Tang M-X. Super-resolution ultrasound imaging. Ultrasound Med Biol 2020;46:865–91.
[16] Huang D, Swanson EA, Lin CP, Schuman JS, Stinson WG, Chang W, Hee MR, Flotte T, Gregory K, Puliafito CA. Optical coherence tomography. Science 1991; 254:1178–81.
[17] Levine A, Wang K, Markowitz O. Optical coherence tomography in the diagnosis of skin cancer. Dermatol Clin 2017;35:465–88.
[18] Ulrich M, Themstrup L, de Carvalho N, Manfredi M, Grana C, Ciardo S, Kästle R, Holmes J, Whitehead R, Jemec GB. Dynamic optical coherence tomography in dermatology. Dermatology 2016;232:298–311.
[19] Tsai M-T, Lee H-C, Lee C-K, Yu C-H, Chen H-M, Chiang C-P, Chang C-C, Wang Y-M, Yang C. Effective indicators for diagnosis of oral cancer using optical coherence tomography. Opt Express 2008;16:15847–62.
[20] Kut C, Chaichana KL, Xi J, Raza SM, Ye X, McVeigh ER, Rodriguez FJ, Quiñones-Hinojosa A, Li X. Detection of human brain cancer infiltration ex vivo and in vivo using quantitative optical coherence tomography. Sci Transl Med 2015;7. 292ra100-292ra100.
[21] Abd El-Sadek I, Miyazawa A, Shen LT-W, Makita S, Fukuda S, Yamashita T, Oka Y, Mukherjee P, Matsusaka S, Oshika T. Optical coherence tomography-based tissue dynamics imaging for longitudinal and drug response evaluation of tumor spheroids. Biomed Opt Express 2020;11:6231–48.
[22] De Boer JF, Hitzenberger CK, Yasuno Y. Polarization sensitive optical coherence tomography–a review. Biomed Opt Express 2017;8:1838–73.
[23] de Boer JF, Milner TE, van Gemert MJC, Nelson JS. Two-dimensional birefringence imaging in biological tissue by polarization-sensitive optical coherence tomography. Opt Lett 1997;22:934–6.
[24] Hariri LP, Adams DC, Applegate MB, Miller AJ, Roop BW, Villiger M, Bouma BE, Suter MJ. Distinguishing tumor from associated fibrosis to increase diagnostic biopsy yield with polarization-sensitive optical coherence tomography. Clin Cancer Res 2019;25:5242–9.
[25] Strasswimmer J, Pierce MC, Park H, Neel V, De Boer JF. Polarization-sensitive optical coherence tomography of invasive basal cell carcinoma. J Biomed Opt 2004;9:292–8.
[26] Duan L, Marvdashti T, Lee A, Tang JY, Ellerbee AK. Automated identification of basal cell carcinoma by polarization-sensitive optical coherence tomography. Biomed Opt Express 2014;5:3717–29.
[27] Marvdashti T, Duan L, Aasi SZ, Tang JY, Bowden AKE. Classification of basal cell carcinoma in human skin using machine learning and quantitative features captured by polarization sensitive optical coherence tomography. Biomed Opt Express 2016;7:3721–35.
[28] Li Y-Q, Chiu K-S, Liu X-R, Hsiao T-Y, Zhao G, Li S-J, Lin C-P, Sun C-W. Polarization-sensitive optical coherence tomography for brain tumor characterization. IEEE J Sel Top Quantum Electron 2019;25:1–7.
[29] South FA, Chaney EJ, Marjanovic M, Adie SG, Boppart SA. Differentiation of ex vivo human breast tissue using polarization-sensitive optical coherence tomography. Biomed Opt Express 2014;5:3417–26.
[30] Hitzenberger CK, Götzinger E, Sticker M, Pircher M, Fercher AF. Measurement and imaging of birefringence and optic axis orientation by phase resolved polarization sensitive optical coherence tomography. Opt Express 2001;9:780–90.
[31] Roth JE, Kozak JA, Yazdanfar S, Rollins AM, Izatt JA. Simplified method for polarization-sensitive optical coherence tomography. Opt Lett 2001;26:1069–71.
[32] C.F. Bohren, D.R. Huffman, Absorption and scattering of light by small particles, John Wiley & Sons2008.
[33] Yan F, Gunay G, Valerio TI, Wang C, Wilson JA, Haddad MS, Watson M, Connell MO, Davidson N, Fung K-M. Characterization and quantification of necrotic tissues and morphology in multicellular ovarian cancer tumor spheroids using optical coherence tomography. Biomed Opt Express 2021;12:3352–71.
[34] Böhringer H, Boller D, Leppert J, Knopp U, Lankenau E, Reusche E, Hüttmann G, Giese A. Time-domain and spectral-domain optical coherence tomography in the analysis of brain tumor tissue. Lasers Surg Med: Off J Am Soc Laser Med Surg 2006; 38:588–97.
[35] Barwari K, de Bruin DM, Cauberg EC, Faber DJ, van Leeuwen TG, Wijkstra H, de la Rosette J, Laguna MP. Advanced diagnostics in renal mass using optical coherence tomography: a preliminary report. J Endourol 2011;25:311–5.
[36] Xiong Y-Q, Mo Y, Wen Y-Q, Cheng M-J, Huo S-T, Chen X-J, Chen Q. Optical coherence tomography for the diagnosis of malignant skin tumors: a meta-analysis. J Biomed Opt 2018;23:020902.
[37] Katta N, Estrada AD, McElroy AB, Gruslova A, Oglesby M, Cabe AG, Feldman MD, Fleming RD, Brenner AJ, Milner TE. Laser brain cancer surgery in a xenograft model guided by optical coherence tomography. Theranostics 2019;9:3555.
[38] Gounis MJ, Ughi GJ, Marosfoi M, Lopes DK, Fiorella D, Bezerra HG, Liang CW, Puri AS. Intravascular optical coherence tomography for neurointerventional surgery. Stroke 2019;50:218–23.
[39] Ehlers JP, Uchida A, Srivastava SK. The integrative surgical theater: combining intraoperative optical coherence tomography and 3D digital visualization for vitreoretinal surgery in the DISCOVER study. Retina 2018;38:S88–96.
[40] Siddiqui M, Nam AS, Tozburun S, Lippok N, Blatter C, Vakoc BJ. High-speed optical coherence tomography by circular interferometric ranging. Nat Photonics 2018;12: 111–6.
[41] Vakoc BJ, Lanning RM, Tyrrell JA, Padera TP, Bartlett LA, Stylianopoulos T, Munn LL, Tearney GJ, Fukumura D, Jain RK. Three-dimensional microscopy of the tumor microenvironment in vivo using optical frequency domain imaging. Nat Med 2009;15:1219–23.
[42] Barwari K, de Bruin DM, Faber DJ, van Leeuwen TG, de la Rosette JJ, Laguna MP. Differentiation between normal renal tissue and renal tumours using functional optical coherence tomography: a phase I in vivo human study. BJU Int. 2012;110: E415–20.
[43] J. Wierwille, Optical coherence tomography as a diagnostic tool in renal transplant and cancer imaging, 2011.
[44] Lamadé W, Glombitza G, Fischer L, Chiu P, Cárdenas Sr CE, Thorn M, Meinzer H-P, Grenacher L, Bauer H, Lehnert T. The impact of 3-dimensional reconstructions on operation planning in liver surgery. Arch Surg 2000;135:1256–61.
[45] Soler L, Nicolau S, Pessaux P, Mutter D, Marescaux J. Real-time 3D image reconstruction guidance in liver resection surgery. Hepatobil Surg Nutr 2014;3:73.
[46] Molitor T, Traktman P. Molecular genetic analysis of VRK1 in mammary epithelial cells: depletion slows proliferation in vitro and tumor growth and metastasis in vivo. Oncogenesis 2013;2. e48-e48.
[47] Tie J, Wang Y, Tomasetti C, Li L, Springer S, Kinde I, Silliman N, Tacey M, Wong H-L, Christie M. Circulating tumor DNA analysis detects minimal residual disease and predicts recurrence in patients with stage II colon cancer. Sci Transl Med 2016;8. 346ra392-346ra392.
[48] Stoecklein NH, Hosch SB, Bezler M, Stern F, Hartmann CH, Vay C, Siegmund A, Scheunemann P, Schurr P, Knoefel WT. Direct genetic analysis of single disseminated cancer cells for prediction of outcome and therapy selection in esophageal cancer. Cancer Cell 2008;13:441–53.
[49] Munivenkatappa R, Schweitzer E, Papadimitriou J, Drachenberg C, Thom K, Perencevich E, Haririan A, Rasetto F, Cooper M, Campos L. The Maryland aggregate pathology index: a deceased donor kidney biopsy scoring system for predicting graft failure. Am J Transplant 2008;8:2316–24.
[50] Philosophe B, Malat GE, Soundararajan S, Barth RN, Manitpisikul W, Wilson NS, Ranganna K, Drachenberg CB, Papadimitriou JC, Neuman BP. Validation of the Maryland Aggregate Pathology Index (MAPI), a pre-implantation scoring system that predicts graft outcome. Clin Transpl 2014;28:897–905.
[51] Kovacs G, Akhtar M, Beckwith BJ, Bugert P, Cooper CS, Delahunt B, Eble JN, Fleming S, Ljungberg B, Medeiros LJ. The Heidelberg classification of renal cell tumours. J Pathol: J Pathol Soc Great Britain Ireland 1997;183:131–3.
[52] Delahunt B, Eble JN. Papillary renal cell carcinoma: a clinicopathologic and immunohistochemical study of 105 tumors. Mod Pathol 1997;10:537–44.
[53] Akhtar M, Al-Bozom IA, Al Hussain T. Papillary renal cell carcinoma (PRCC): an update. Adv Anat Pathol 2019;26:124–32.
[54] Ding Z, Liang C-P, Chen Y. Technology developments and biomedical applications of polarization-sensitive optical coherence tomography. Front Optoelectron 2015; 8:128–40.
[55] Gräfe MG, van de Kreeke JA, Willemse J, Braaf B, de Jong Y, Tan HS, Verbraak FD, de Boer JF. Subretinal fibrosis detection using polarization sensitive optical coherence tomography. Transl Vis Sci Technol 2020;9. 13-13.
[56] Braaf B, Vermeer KA, de Groot M, Vienola KV, de Boer JF. Fiber-based polarization-sensitive OCT of the human retina with correction of system polarization distortions. Biomed Opt Express 2014;5:2736–58.
[57] Villiger M, Lorenser D, McLaughlin RA, Quirk BC, Kirk RW, Bouma BE, Sampson DD. Deep tissue volume imaging of birefringence through fibre-optic needle probes for the delineation of breast tumour. Sci Rep 2016;6:1–11.
[58] Feroldi F, Willemse J, Davidoiu V, Gräfe MG, van Iperen DJ, Goorsenberg AW, Annema JT, Daniels JM, Bonta PI, de Boer JF. In vivo multifunctional optical coherence tomography at the periphery of the lungs. Biomed Opt Express 2019;10: 3070–91.
[59] Willemse J, Gräfe MG, van de Kreeke JA, Feroldi F, Verbraak FD, De Boer JF. Optic axis uniformity as a metric to improve the contrast of birefringent structures and analyze the retinal nerve fiber layer in polarization-sensitive optical coherence tomography. Opt Lett 2019;44:3893–6.